scientific reports

Check for updates

OPEN

Plasmonic imaging of living pancreatic beta-cell networks

Sidahmed Abayzeed[1]✉, Daniel Galvis[2], Karen Regules Medel[1], Catarina F. Jones[3,4], Oscar Barajas Gonzalez[1], Kerry Setchfield[1], Rosalia Moreddu[3,4], Michael G. Somekh[1], Kyle C. A. Wedgwood[5,6] & Paul Smith[7]

We present a novel plasmonic imaging technique for real-time, label-free tracking of bioelectrical interactions in live pancreatic beta-cell networks. Surface plasmon resonance microscopy (SPRM) is utilized to reveal synchronized glucose-induced intensity oscillations that are suppressed by calcium channel blockers. These oscillations are observed at the subcellular scale with a resolution of 1 µm. The technique can also uncover the extracellular spread of these oscillations beyond the cells. We further combine SPRM with network analysis to quantify coordinated electrical activity within the living cell network using both amplitude and phase-based metrics. Our results demonstrate a new method for studying electrical communication in pancreatic beta-cells, which could be crucial for understanding dysregulation in diabetes and advancing treatment development. This technique holds promise for investigating electrical connectivity in biological cell networks with applications in neuroscience, cardiac science, and bioelectricity in cancer, microbiology, development and regeneration.

Keywords Label-free plasmonic microscopy, Bioelectrical networks, Pancreatic beta cells, Diabetes, Bioelectrical and calcium signalling, Bioelectricity

Biological cells have evolved complex molecular mechanisms for coordinated electrical signaling that are critical for a wide range of physiological and developmental processes. For example, neurons form networks to process sensory information[1] and coordinate the organism's interactions with internal[2] and external[3] environments. Similarly, cardiomyocytes are electrically coupled via gap junctions to produce synchronous mechanical action[4]. Hormone secreting cells also function in synchronized networks driven by coupled electric oscillations to produce secretions that are efficient for their function. For instance, pancreatic beta-cells, within the islet of Langerhans, are functionally connected[5], a feature crucial for regulated insulin release and glucose homeostasis[5]. Furthermore, intercellular electrical communications via tunnelling nanotubules are reported in immune cells[6]. More recently, novel oscillations of membrane potentials have been observed in human breast cancer cells with notable temporal correlations[7]—indicative of electrical coupling. Furthermore, a recent breakthrough revealed the role of electrical excitability in the progression of small-cell lung cancer[8]. Similar to eukaryotic cells, prokaryotes coordinate metabolism via propagation of electrical signals in microbial biofilms[9]. These examples highlight the significance of tracking electrical signals in live cells.

Electrical coupling in living biological cells is currently investigated via microelectrode arrays (MEAs)[10] and probes[11], which provide a direct measure of endogenous electrical signaling. However, MEAs and high density MEAs offer a limited spatial resolution (i.e. several micrometers) and low spatial sampling due to the constraints of fabrication, electrical wiring and electrode spacing[12]. Calcium and voltage imaging approaches are also employed to monitor synchronization of oscillations in intracellular calcium and transmembrane potential. However, these imaging approaches suffer from the drawbacks associated with fluorescence, such as limited temporal resolution and sensitivity. Although these technologies have driven a great advancement in our understanding of living cell networks[13,14], there is a need for new technology with enhanced capabilities that offer label-free, high-resolution and high-density characterization of electrical connectivity in living cells.

The development of label-free methods has allowed measurement of electrical signals in vitro and in vivo. For instance, plasmonic approaches have been applied to track action potentials in neurons[15,16] and cardiomyocytes[17]. Furthermore, nitrogen vacancy diamond sensors[18,19], and graphene sensors[20] have also been introduced for label-free detection of electrical signaling in living neurons. Building on this foundation, we introduce a novel

[1]Faculty of Engineering, University of Nottingham, Nottingham, UK. [2]Centre for Systems Modelling & Quantitative Biomedicine (SMQB), School of Medical Sciences, University of Birmingham, Birmingham, UK. [3]School of Electronics and Computer Science, University of Southampton, Southampton, UK. [4]Institute for Life Sciences, University of Southampton, Southampton, UK. [5]Living Systems Institute, University of Exeter, Exeter, UK. [6]EPSRC Hub for Quantitative Modelling in Healthcare, University of Exeter, Exeter, UK. [7]School of Life Sciences, University of Nottingham, Nottingham, UK. ✉email: sidahmed.abayzeed2@nottingham.ac.uk

approach that shifts the focus to coordinated behaviour of pancreatic beta cells, serving as a model for network-level activity. Our technique captures bioelectrical activity at the sub-cellular level with a spatial resolution of 1 μm^2, while simultaneously providing a view of the entire network. Unlike previous methods, our technique uniquely reveals how activity propagates through the extracellular space, extending analysis beyond direct cell-sensor contact. Furthermore, we merge surface plasmon resonance microscopy (SPRM) with network analysis techniques to explore the coordinated network activity and assess the temporal variations in connectivity. This paradigm opens avenues for investigating network coordination in processes such as development, regeneration, and tissue repair, while remaining broadly adaptable to other cell types.

SPRM was introduced in a pioneering work by Rothenhäusler and Knoll[21] and independently by Yeatman and Ash[22] in the late 1980s as a contrast enhancement technique achieved by illuminating biological samples, adhered to a gold or silver thin film, through the excitation of surface plasmons (SPs). Since then, SPRM has been investigated for studying cell adhesion, migration and proliferation in a label-free manner[23]. Furthermore, several studies have demonstrated the ability of SPRM to reveal time-resolved processes[24,25] such as membrane biomolecular interactions[26] and exocytosis[27]. SPRM of various cell types[28] such as neurons, cardiac and bacterial cells[29,30] have driven the interest of several groups globally; further demonstrating its diverse applications[31,32].

The decades of research from several teams have innovated a variety of SPRM configurations and concepts, for instance, leveraging the change in phase[33] or intensity of reflected light around the surface plasmon resonance (SPR) position[34]. This includes highly sensitive interferometric approaches that exploit the sharp phase transitions at the SP excitation angle[35]. The high intensity gradients of the SPR curve, a plot of light reflectivity with a pronounced minimum at the resonance angle, are utilized for realizing widefield SPRM configurations[36,37]. This is achieved by illuminating the sample at an angle of incidence with a non-zero and, ideally, a maximum gradient of SPR curve at a fixed or multiple azimuthal directions[38]. The fixed-angle widefield configuration has been used to investigate cell-sensor interfaces[39] and realize impedance microspectroscopy of cells and biomolecules[40,41]. The output of SPRM, such as changes in reflected light intensity at a high intensity gradient, probes the electric charge dynamics at the metal-electrolyte interface[41]. This capability directly measures the electrical activity of living biological cells[16] due to the ionic perturbation of the double-layer capacitor at the cell sensor interface[42]. We leverage this SPRM capability for fine-grained imaging of electrical activity from the sub-cellular level to a whole cellular network, which is anticipated to provide novel insights about the function of biological cell networks, with cutting-edge applications in cancer, diabetes, neuroscience and microbial colonies.

In this study, we used the pancreatic beta-cell line MIN6. MIN6 are a well-established, representative model, of primary beta-cells[43] and have been used in over 16,000 publications prior to 2025. They share the hallmarks of native beta-cells: glucose sensitive calcium-dependent action potentials, which are responsive to specific hormones and ion-channel drugs and are coupled to insulin secretion[44]. Pancreatic beta-cells produce action potential electrical behaviour in response to an elevation in blood glucose[45]. Briefly, a rise in plasma glucose inhibits the activity of ATP-sensitive potassium channels (KATP), which is predominantly responsible for their resting membrane potential, Vm of -70 mV. This leads to depolarisation of Vm and activation of voltage-gated Ca2 + channels (VGCCs) and calcium-dependent action potential (AP) electrical activity (+ 20 mV peak). The frequency of APs is graded with glucose concentration and degree of KATP block[45], from this an emergent electrical behaviour of bursts or cluster of APs arises. Bursting consists of APs solely associated with depolarized, plateau Vm of ~ -40mV separated by periods of electrically silent hyperpolarized Vm of ~ -50mV[46]. The molecular identity, expression profile, pharmacology, roles and regulation of KATP and the VGCCs within the pancreatic beta-cell are well documented[47].

Results

Surface plasmon resonance microscopy (SPRM) of pancreatic beta-cells

We present SPRM applied to the imaging of live cell networks, introducing the capability to monitor cellular interactions as well as the signal spread in their vicinity, for the first time. This is crucial to elucidate the propagation of information between cells embedded in a conductive extracellular environment. To achieve this, we fabricated SPR sensors based on gold thin films, as depicted in Fig. 1a, to excite SPs at the metal–dielectric interface. The resonance phenomenon is marked by a drop of reflectivity at a particular angle of incidence, termed SPR angle. Research has shown that this resonance position is sensitive to refractive index variations at the interface and our group has investigated SPR sensitivity to externally applied voltage[42,48]. We have reported detecting short millisecond voltage pulses indicating a detection limit as low as 10 mV[42]. The ability to optically measure voltage in a label-free manner opens new avenues in imaging bioelectrical signals at subcellular levels.

To demonstrate the SPRM applications in studying cell networks, the MIN6 immortalized cell line was chosen as an in vitro model of beta-cells and transferred to Hanks balanced salt solution (HBSS), as detailed in the Methods section, using poly-L-lysine (PLL) treated gold thin films as a substrate. To probe the cell sensor interface, we utilized the SPRM configuration illustrated in brief in Fig. 1a and detailed in the Methods section. In this paper, we employed a widefield setup using a high numerical aperture oil immersion objective lens to excite SPs at an angle of incidence greater than that of the total internal reflection. The angle of incidence can be tuned by laterally translating a focus on the back focal plane of the objective lens.

To provide functional imaging capabilities, this configuration used an off-resonance angle of incidence for illumination where a subtle shift in resonance angle leads to a widefield change in the intensity of reflected light. Since, the aim of this study is to track both cells and their surrounding extracellular background, a careful selection of the angle of illumination will maximize the information retrieval. Therefore, we employed a transfer matrix-based simulation of the cell sensor interface to inform the choice of angle of incidence. Simulating the cell sensor interface, demonstrated in Fig. 1b, produces the SPR curves corresponding to the cell and the background as presented in Fig. 1c. A visual inspection shows that the points of high structural contrast (i.e., ii, and iv in Fig. 1e) have the lowest functional sensitivities for both cells and background. Functional sensitivity

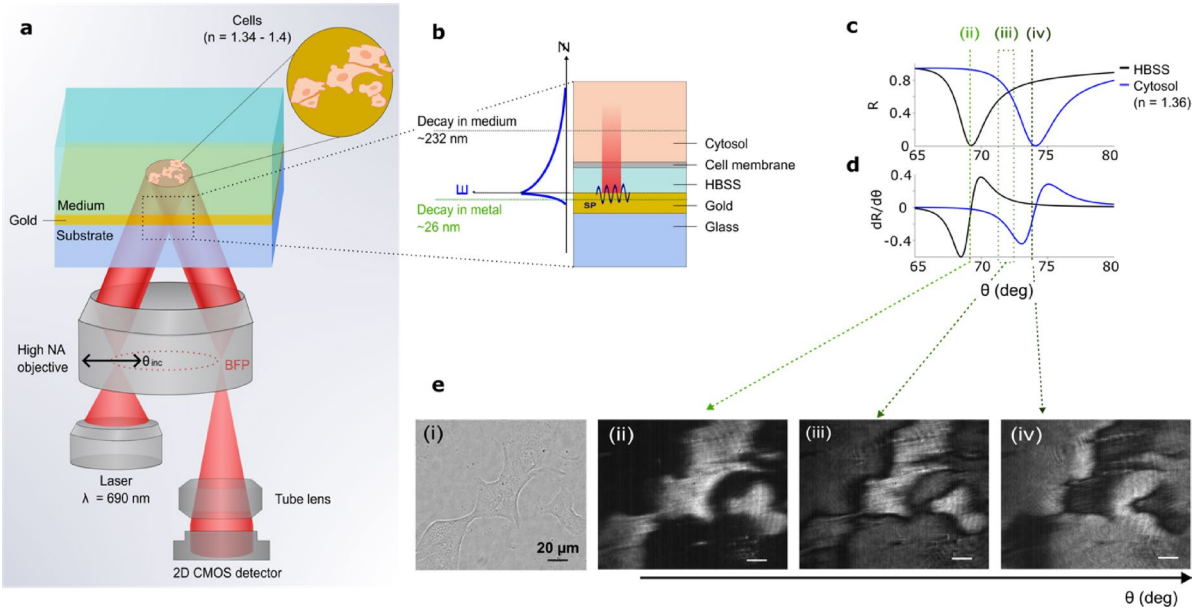

Fig. 1. Surface Plasmon Resonance Microscopy (SPRM) of pancreatic beta-cells (**a**) Schematic presenting the experimental setup for SPRM, depicting the layered structure of gold thin film on glass substrate with cells adhered to the gold surface in Hanks' balanced salt solution (HBSS). A fiber-coupled laser (690 nm) is collimated before focusing on the back focal plane (BFP) of a high numerical aperture oil immersion objective to produce a collimated beam at the sample. The angle of illumination is varied by laterally scanning the focus on the BFP. The sample is imaged using a 2D CMOS pixelated detector. (**b**) A magnified view of the SPR sensor and cell interface showing the interface layers (glass, Au thin film of 50 nm, medium (HBSS), cell membrane of *c*.7 nm thickness, and cytosol), with an illustration of the penetration depth of SPs in both metal and dielectric media. This indicates sensitivity to the cell membrane and the proximal intra- and extracellular spaces. (**c**) SPR curves presenting the reflection coefficient for various angles of incidence, simulated for bare gold with HBSS and for the gold-cell interface respectively. (**d**) The corresponding first derivative of reflectivity with respect to the angle of incidence, showing the variations in the sensitivity of the measurement for optimising the angle of illumination. (**e**) (i). Brightfield microscopy image of live MIN6 beta-cells cultured on PLL-modified Au thin film. e (ii), e (iii), and e (iv) are the corresponding SPRM images at different angles of illumination. The angle of incidence is selected in region iii, although this gives reduced sensitivity, it allows simultaneous tracking of cells and the extracellular regions where cells are not present on the sensor.

is defined, here, as the ability to resolve small changes in the resonance angle or intensity due to dynamic living processes, which is realized by selecting an angle of illumination at a non-zero gradient of the SPR curve. The selection of an angle of incidence around the intersection of the two SPR curves allows signal dynamics to be probed with coverage of both cells and the surroundings. Nevertheless, this operating point (region iii in Fig. 1c and d) does not necessarily provide the maximum sensitivities for both the cell and the background individually or the highest structural contrast. The cell-sensor interface is captured at different angles of incidence to illustrate the concept of functional sensitivity, as presented in Fig. 1e.

We have previously presented a method based on mapping intensity gradient that can translate the change in intensity to the corresponding resonance angle shift[41]. However, since for this study we are only interested in information propagation within the cell network, where connectivity is revealed using only correlations of phase and amplitudes, therefore, oscillation intensity was not quantitatively linked to the resonance angle shift. The next section shows the utilization of the SPRM approach to track the bioelectrical behaviour of pancreatic beta-cells.

SPRM reveals synchronized oscillations in beta-cell networks

We report synchronized sub-second intensity oscillations in both cells and their extracellular background in the presence of HBSS supplemented with 10 mM glucose. We conjecture that the observed oscillations are linked to ionic currents associated with glucose-induced electrical signaling in pancreatic beta-cells, an idea which is validated in the next section. Coordinated electrical oscillations in pancreatic cells are well known to underpin the secretion of insulin by pancreatic islets[45,49]. Figure 2 shows a cluster of three MIN6 cells, with bright-field and SPRM images in Fig. 2a and b, respectively.

Synchronous intensity oscillations are observed from regions of interest (ROIs) 1–5 where each ROI represents either a cell or the background. ROIs 1–3 (cells) display oscillations that appear anticorrelated with those from ROIs 4 and 5 (extracellular background), as shown in Fig. 2c. However, this anticorrelation is not physiological but results from the experimental conditions. In particular, the sample is illuminated with a collimated beam at a fixed angle of incidence, and due to refractive index differences, cells and their surroundings have different

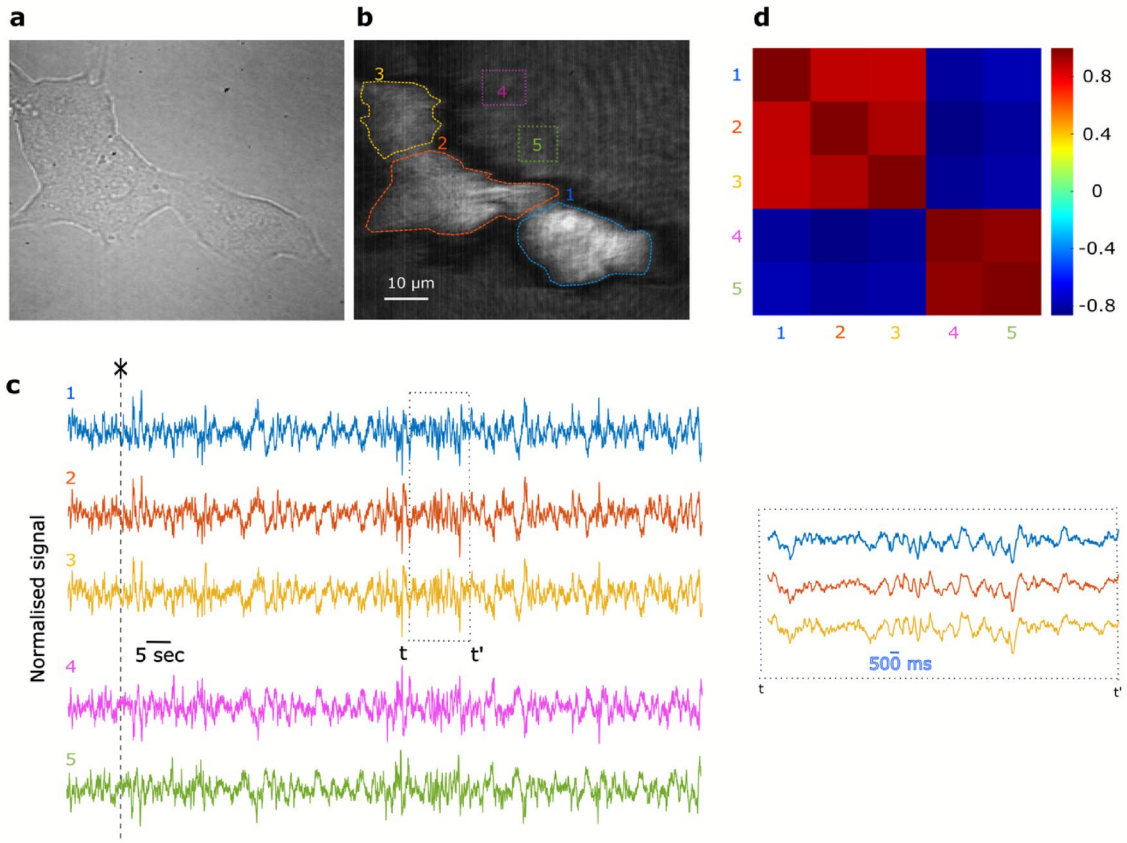

Fig. 2. SPRM reveals correlated oscillations in pancreatic beta-cells. (**a**) Brightfield image of MIN6 cells cultured on PLL-modified Au thin film. (**b**) Corresponding SPRM image with five regions of interest highlighting cells (1, 2 and 3) and the extracellular background (4 and 5). (**c**) Time-resolved reflectivity recorded over 130 s in HBSS with 10 mM glucose for the five regions shown in (**b**), inset shows a magnified view of a selected time window, indicated by t to t', for the three cells which shows synchronised intensity oscillations. Traces appear synchronised but the background ROIs are anticorrelated. (**d**) Heat map displaying the correlation between signals extracted from ROIs 1 – 5 investigating signaling at the cellular ROIs (1–3) and the background ROIs (4, 5), where cells are not present.

resonance positions. As a result, the chosen angle of illumination leads to opposite intensity gradients between the cells and background (Fig. 1c and d), as discussed in the previous section. Therefore, correlated resonance position dynamics, between the cells and their background, lead to anticorrelated intensity changes.

This observation suggests that the SPR angle dynamics for both cells and the extracellular background are driven by the same biophysical process, which would lead to a correlated resonance angle shift. Pearson's cross-correlation between these channels (i.e. ROIs 1—5) was computed and displayed in Fig. 2d showing two averages of 0.9067 ± 0.0367 and -0.8503 ± 0.0218. This correlation map confirms that the oscillations are highly correlated within cells and extracellular background channels; however, there is anticorrelation between the two groups due to the SPR sensor transfer function.

Synchronous electrical oscillations are frequently observed in pancreatic beta-cell networks. To validate the SPRM-detected oscillations shown in Fig. 2 against established techniques, we conducted intracellular calcium imaging in MIN6 cells (Fig. 3a) – the same cell line employed for SPRM studies – which revealed synchrony comparable to that observed with SPRM. As shown in Fig. 3b and c, multiple cell clusters displayed highly correlated oscillatory activity, further confirming the electrophysiological relevance of the oscillations identified by SPRM.

Fluorescent-based calcium and voltage imaging methods are limited to labelled cells, whereas SPRM reveals signals from both the cells and the extracellular background – an important consideration from an electrophysiology perspective. This new capability allows a thorough investigation of electrical signal propagation in pancreatic beta-cells and the surrounding medium. Although monitoring both cells and background is possible with microelectrode arrays, this is achieved at a reduced spatial resolution, of several micrometers enforced by the electrode spacing, even with high-density arrays[12].

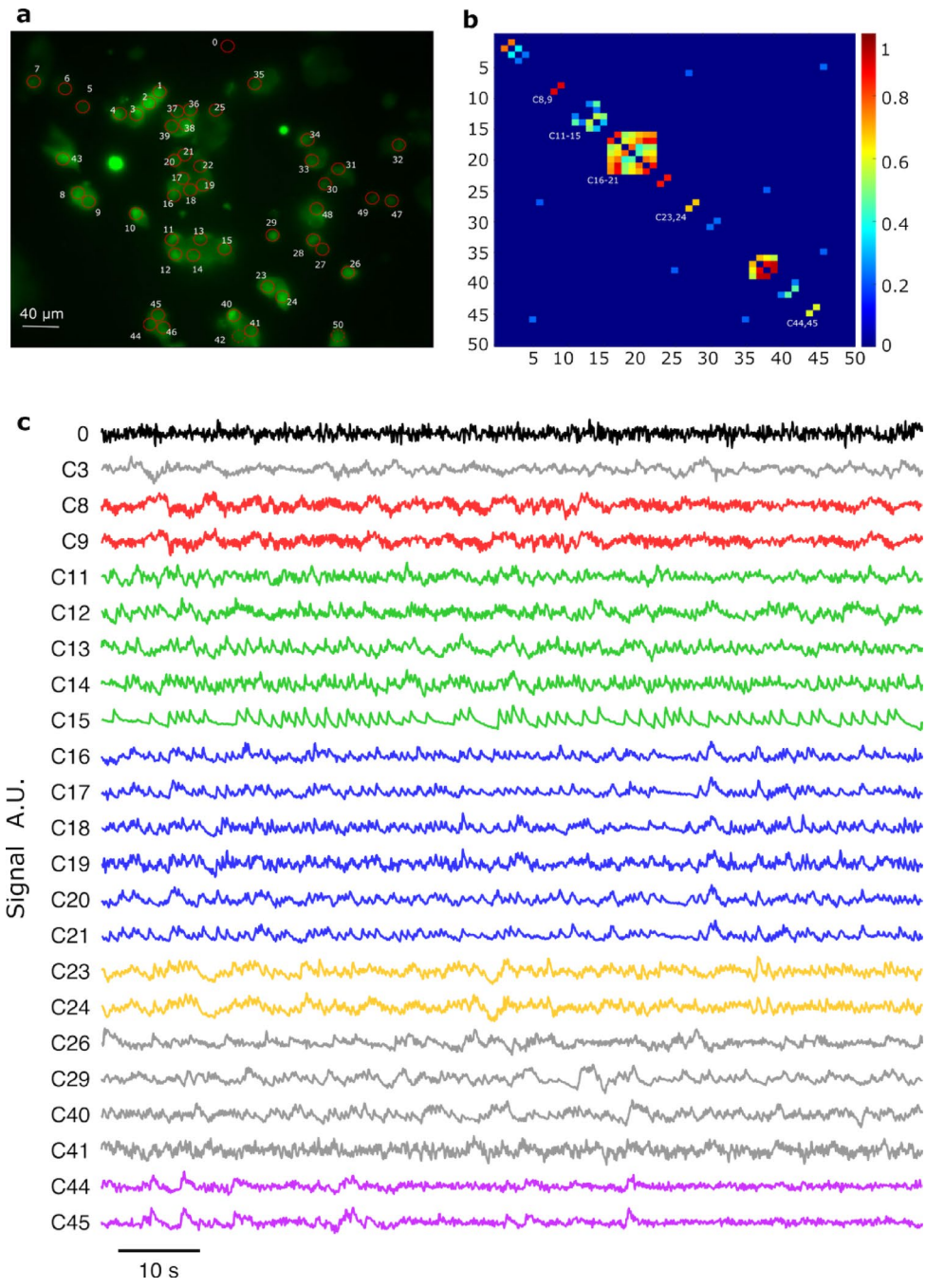

Fig. 3. Intracellular calcium oscillations in pancreatic beta cells within HBSS supplemented with 10 mM glucose. (**a**) Fluorescence image of MIN6 cells loaded with FLUO-4, excited at 450–490 nm, with 0–50 regions of interest (ROIs) indicated (0 denotes the background). Average fluorescence image of 3,000 frames of a field of MIN6 cells, with each measured cell labelled to indicate its 2D geography. (**b**) Cross-correlation matrix showing the Pearson correlation coefficients (threshold of 0.3) calculated between ROIs 0–50. (**c**) Exemplary 100-s traces of selected ROIs (band-pass filtered between 0.1 and 5 Hz), including clusters with high correlation {C8, C9}, {C11– C15}, {C16–C21}, {C23, C24}, {C44, C45}, alongside other ROIs selected at random.

SPRM resolves subcellular oscillations in beta cells

SPRM provides an ultra-high-density recording capability, not previously possible, as demonstrated in Fig. 4. Here we show that these oscillations can be extracted from subcellular regions as small as 1 μm^2. The spatial resolution of SPRM is diffraction limited in the direction perpendicular to SPs propagation while it is reduced to approximately 3 µm along the propagation direction[50]. Therefore, while the method can report the global response from a ROI that averages over a whole cell, signals from subcellular regions can also be uncovered. To demonstrate this capability, the field of view was segmented into multiple channels, labelled (j, i) in Fig. 4a, each

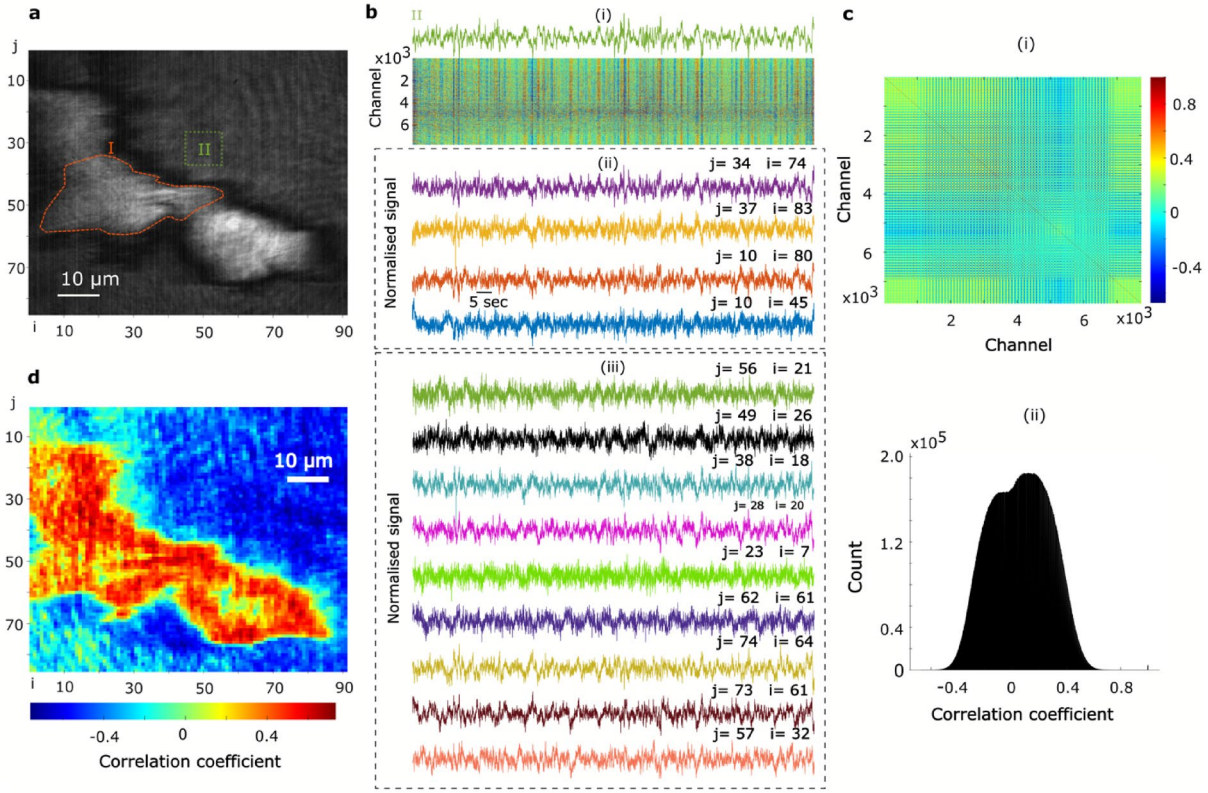

Fig. 4. SPRM uncovers high-resolution sub-cellular oscillations in pancreatic beta-cells. (**a**) SPRM image highlighting two ROIs: I and II corresponding to a cell and the extracellular background, respectively. The image is segmented into multiple channels (pixels) of 1 μm^2 labelled (i,j). (**b**) A stack of channels demonstrating ultra-high-density recording of normalized intensity oscillations with a resolution of 1 μm^2, shown in b(i). Exemplar traces are presented in b(ii) and b(iii) for the background and cell channels, respectively. (**c**) Pearson's cross-correlation between the ultra-high-density channels, mapped in c(i) with the corresponding histogram depicted in c(ii). In b(i) and c(i), the cells are located between channels 4000 and 6000. (**d**) The map illustrates the outcome of Pearson's cross-correlation, comparing a signal extracted by averaging an exemplar individual cell (with ROI I used as an example) to the local high-density sub-cellular signals (i.e., channels). This analysis highlights both the spatial and temporal heterogeneity present in the resulting signals.

integrating the intensity within a 1 μm^2 grid element. The small field of few of 85 $\mu m \times 91$ μm is covered by more than 7700 channels, offering an exceptionally high spatial resolution. The correlation between the channels is clearly visible in Fig. 4b(i). Similarly, an anticorrelation between the cells and extracellular recordings is observed when comparing channels 4000 to 6000, where most of the MIN6 cells are located, to the remaining extracellular channels.

The ultra-high-density recording capability can be leveraged to investigate the correlation and synchronization between subcellular signals. To achieve this, Pearson's cross-correlation was computed for the channels described above and the correlation statistics are presented using the correlation map and the histogram in Fig. 4c(i) and c(ii), respectively. To rule out the possibility that reduced signal-to-noise ratio in the subcellular regions caused low correlations, we extracted the envelope of the oscillations using Hilbert transform (HT) before smoothing (see Methods section). This approach produced a correlation distribution similar to that obtained prior to envelope extraction and smoothing, ruling out low SNR as the source of reduced correlations (Supplementary Information, Fig. S2). We emphasize that envelope extraction via HT followed by smoothing enhances the SNR. Moreover, strong correlations are also apparent at the single-pixel level in the extracellular background channels (Fig. S2b), confirming that the observed differences in correlation are robust and not merely the result of noise.

Next, we investigated the spatial origin and propagation of the observed intensity oscillations. Figures 2 and 4 illustrate global correlation between the MIN6 cells compared to local correlation statistics, obtained at the subcellular levels. Global correlations are defined as those between ROIs covering entire individual cells, while local correlations refer to those between subcellular signals. While the signals extracted by integrating over individual MIN6 cells (ROIs: 1–3) are highly correlated, as shown in Fig. 2d, the subcellular signals show a lower correlation that is distributed over a range of -0.5 to 0.7, as presented in Fig. 4c(i) and c(ii). To visualise the subcellular correlations spatially, we calculated cross correlations between a global signal, integrated over a ROI covering an entire single cell (e.g. region I in Fig. 4a), and the signals extracted from the 1 μm^2 sized channels

shown in Fig. 4b(i). The resulting global–local cross correlation map is presented in Fig. 4d. A strong correlation is seen in the extracellular space surrounding cells, likely resulting from constructive interference between these cell-originated signals. On the other hand, the cellular recordings exhibit a relatively heterogeneous correlations, with higher correlations around the edge of the cells, in comparison to the central regions, indicating the spatial origin of the obtained signals. Representative time-series from cells and their background extracellular channels are presented in Fig. 4b(ii) and b(iii), the channel index i, j refers to the columns and rows that indicate the pixel location in the map in Fig. 4a.

Synchronized intensity oscillations are suppressed via calcium channel blockers

To investigate the origin of the intensity oscillations, MIN6 cells were studied under three conditions consecutively: 1) baseline HBSS in the absence of glucose; (2) HBSS supplemented with 10 mM glucose; and 3) HBSS supplemented with 10 mM glucose and 40 µM of the calcium channel blocker nifedipine, as shown in Fig. 5. To compare the oscillation amplitudes, time series data from each cell were normalized to their respective

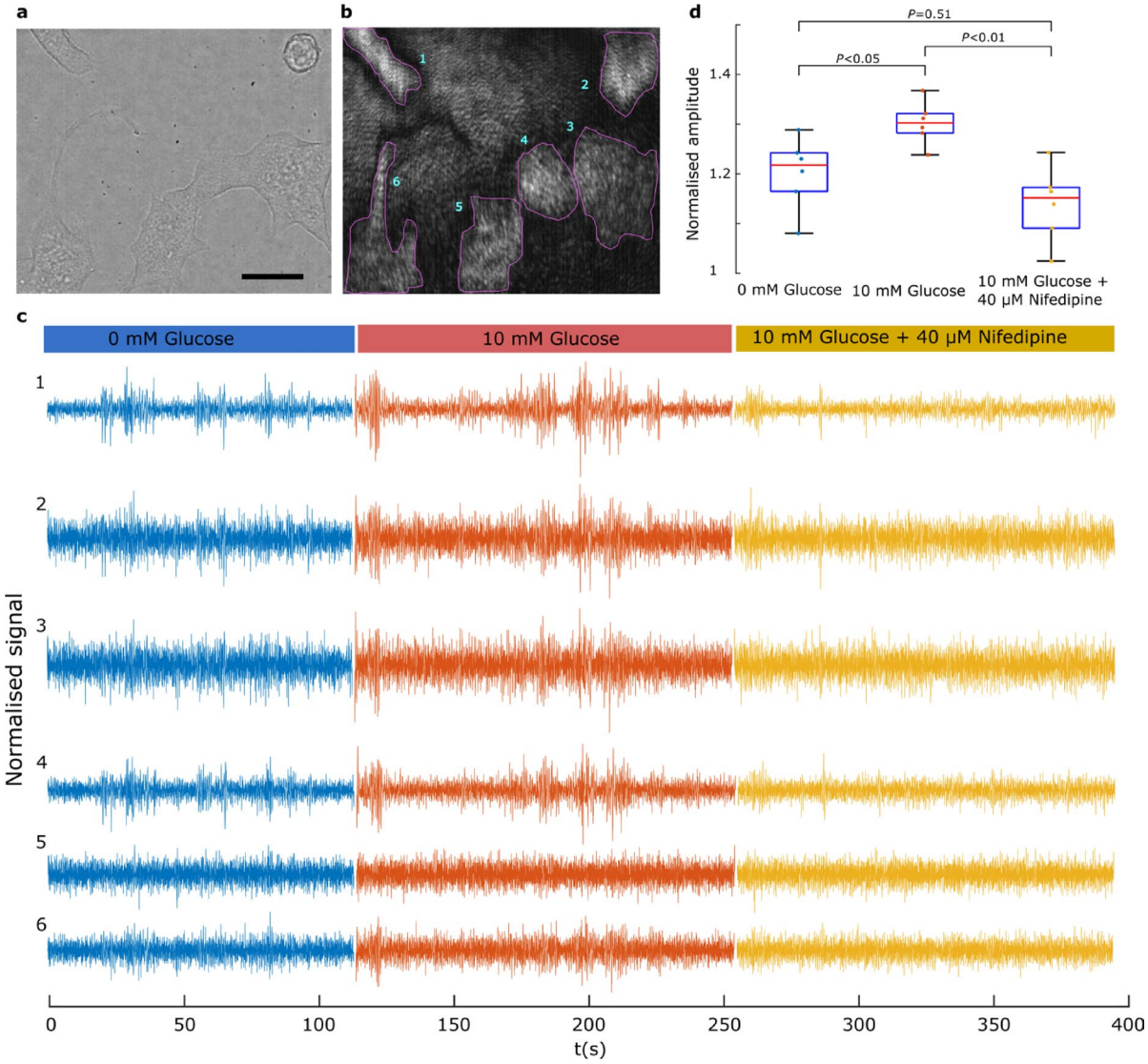

Fig. 5. Synchronised network oscillations are suppressed in the presence of a calcium channel blocker. (**a**) Brightfield image of MIN6 cells cultured on PLL-modified Au thin film. Scale bar 10 µm. (**b**) Corresponding SPRM image with 6 cellular regions of interest. (**c**) Time-series recordings from the six cellular ROIs presenting time-resolved reflectivity, under treatment with: 1) Hanks balanced salt solution (HBSS) without glucose; 2) HBSS supplemented with 10 mM glucose; and 3) HBSS supplemented with 10 mM glucose and 40 µM nifedipine. (**d**) Comparison of the effect of the three treatments on cells displaying the average amplitude profiles of the cells. Prior to identifying the amplitude profile, each signal was filtered between 0.1–15 Hz (see Methods) before standardization using the standard deviation over all the three recordings. Pairwise comparisons were performed using paired t-tests, with p-values adjusted for multiple comparisons (n = 6 cells) using the Bonferroni correction. Whiskers extend to 1.5 times the interquartile range (IQR).

standard deviation, calculated across the three experimental conditions. Cells exhibited spontaneous oscillations under baseline conditions, which increased in amplitude upon glucose exposure. However, when treated with nifedipine, the amplitude of these oscillations diminished, as observed in Fig. 5c and d.

The results, presented in Fig. 5, indicate that the oscillations are linked to ionic dynamics across the cell membrane given the observed effect of the calcium channel blocker, nifedipine, which at the concentration used has well documented electrical activity blocking effects in pancreatic beta-cells[51]. The spread of the signals beyond the regions of the cell electrode interface also supports the interpretation of the bioelectrical nature of the observed oscillations. One possible explanation of this latter phenomenon is that transmembrane ion dynamics modulate the charge at the double layer capacitor at the cell sensor interface leading to alteration of electron density in the metal, thus giving rise to the observed oscillations[42]. Similarly, the perturbation of double-layer capacitor by transient increase or depletion of ion species could lead to changes in the refractive index in the dielectric layer adjacent to the metal. Several lines of evidence confirm the observed oscillations represent genuine bioelectrical signals rather than instrument artifacts. First, the observed anticorrelation between cellular and background regions is inconsistent with the common-mode fluctuations from light source or detector that would produce correlated changes across the field of view[52]. Second, the spatial specificity of these oscillations is demonstrated by cell 5- Fig. 5c, which shows no activity while neighbouring cells exhibit oscillations. Third, pharmacological suppression by the calcium channel blocker nifedipine demonstrates biological dependence. Fourth, we demonstrated that exposure to 0.1% saponin, which has a cell-lysing effect, resulted in reduced correlative oscillations compared with HBSS supplemented with a high concentration of 50 mM KCl (see Supplementary Figs. S4 and S5). Finally, MEA and patch clamp recordings of MIN6 cells (Figs. 6 and 7) confirm the suppression of electrical activity patterns under nifedipine treatment.

Figure 6 presents MEA recordings of MIN6 cell electrical activity under three experimental conditions: HBSS baseline, HBSS with glucose stimulation, and HBSS with nifedipine treatment, as detailed in the Methods. Upon exposure to 10 mM glucose, MIN6 cells displayed pronounced extracellular activity in the 1–15 Hz range, reflecting rapid depolarisation–repolarisation events characteristic of beta-cell spiking. This activity was abolished by nifedipine, confirming that the observed oscillations depend on L-type Ca^{2+} channel-mediated bursting. A similar effect was observed using cell-attached patch-clamp recording of action current events where

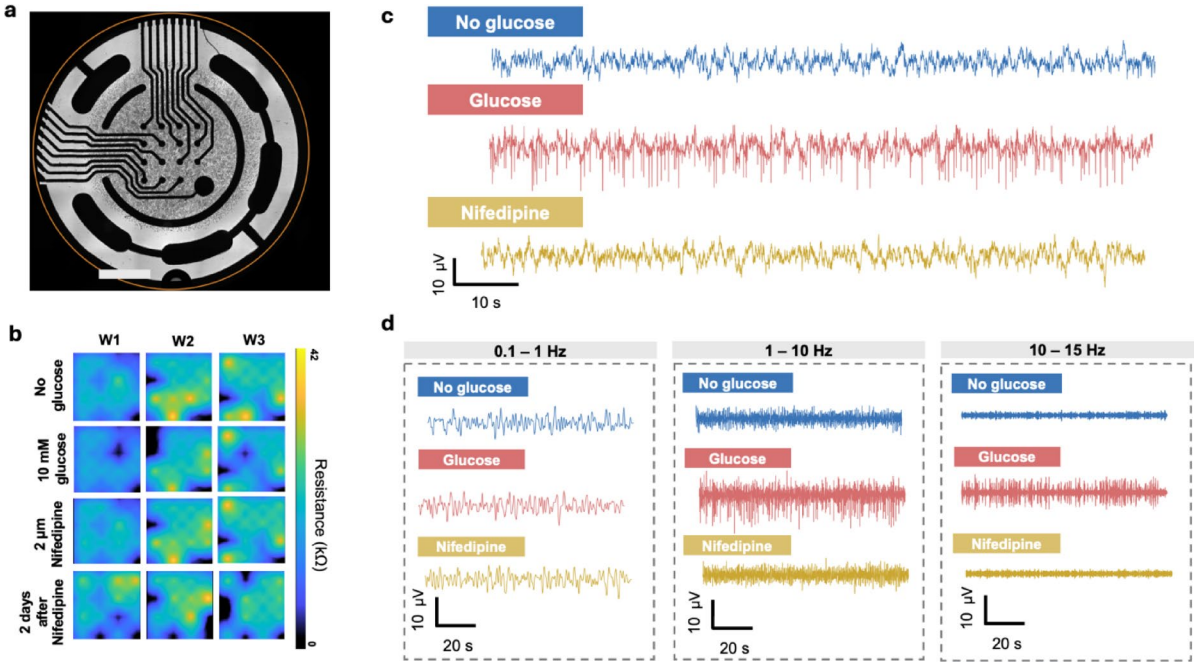

Fig. 6. Glucose modulation of MIN6 electrical behaviour assessed using MEA recordings. (**a**) Bright-field micrograph of the circular microelectrode array used for recordings, displaying the radial arrangement of electrodes and the central culture region where MIN6 cells were seeded. Scale bar = 1000 µm. (**b**) Impedance-based viability maps for three independent wells (W1-W3). Each heatmap shows the impedance magnitude measured at the electrode–cell interface, serving as a surrogate metric for cell coverage and viability. Higher impedance indicates greater cell attachment. The four rows depict: no glucose, 10 mM glucose, 2 µM nifedipine, and two days after nifedipine treatment, illustrating condition-dependent variations in cell viability and adherence. (**c**) Representative 100-s extracellular voltage traces recorded from the same MEA electrode under three conditions: glucose-free HBSS, HBSS supplemented with 10 mM glucose, and HBSS supplemented with 10 mM glucose plus 2 µM nifedipine. The traces, filtered with a standard 0–15 Hz band-pass, reveal condition-dependent variations in the amplitude of MIN6 electrical activity. (**d**) Frequency-resolved decomposition of the same electrode shown in (**a**). Glucose enhances electrical activity, while nifedipine suppresses it within the 1–15 Hz range.

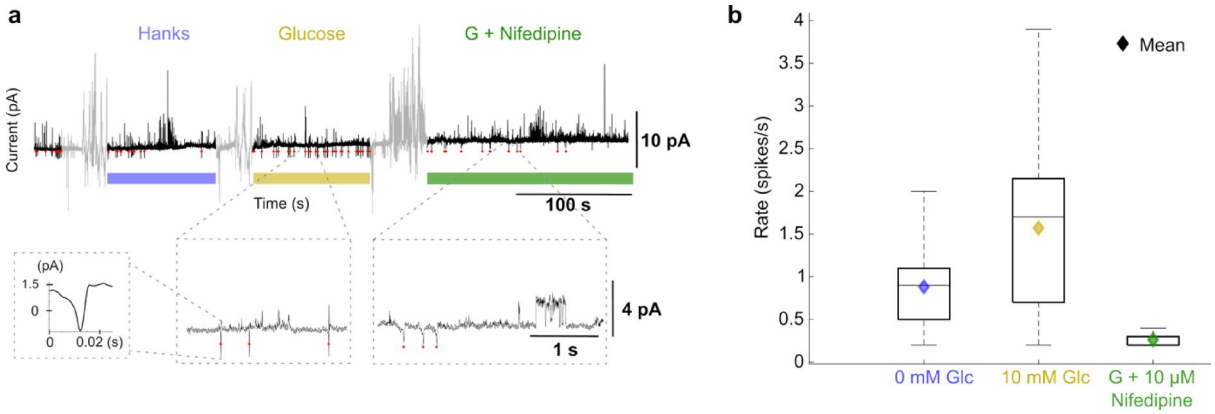

Fig. 7. Cell-attached patch-clamp recordings of glucose-induced activity in a MIN6 β-cell and quantification of spike frequency. (**a**) Representative current trace recorded under three consecutive conditions: HBSS buffer (0 mM glucose), 10 mM glucose, and 10 mM glucose + 10 μM nifedipine. The black trace shows the analysed current, while grey segments correspond to periods of perfusion during which mechanical noise was introduced. Red ticks mark automatically detected downward current deflections identified as action-current events using a dynamic threshold-based detection algorithm (threshold = baseline − 3 × noise; 50 ms refractory period). Coloured horizontal bars indicate the duration of each condition (blue = HBSS, yellow = HBSS + glucose, green = HBSS + glucose + nifedipine). Expanded regions below illustrate zoomed view of spike events during the baseline and glucose phases, with an inset showing a single representative event (amplitude ≈ 3 pA, width ≈ 0.02 ms). (**b**) Quantification of firing activity for the three conditions for three experiments. Each box represents the distribution of windowed spike rates (10-s windows, 2-s step) across three cells analysed (286 spike events). Box edges denote the inter-quartile range (25th–75th percentile); the centre line shows the median; whiskers extend to 1.5 times the IQR. Diamond symbols indicate the mean rate for each condition. Mean ± SEM firing rates were 0.88 ± 0.06 spikes/s for 0 mM glucose, 1.57 ± 0.07 spikes/s for 10 mM glucose, and 0.26 ± 0.02 spikes/s for 10 mM glucose + 10 μM nifedipine. Nifedipine effectively suppressed activity, consistent with its role as a channel blocker.

exposure to glucose has led to increased firing rate, which reduces upon exposure to nifedipine, as presented in Fig. 7. Although these electrode-based electrical recordings were not conducted simultaneously with SPRM, they demonstrate electrical behaviour of MIN6 under similar treatments showing patterns similar to those observed with SPRM.

In the next section, we will demonstrate how these cells behave collectively as a network using techniques from computational graph theory to estimate connectivity across the network. Specifically, we use the phase-locking factor (PLF; explained in the next section) to estimate the influence of intensity oscillations in one cell to those in another.

Functional connectivity in pancreatic cell networks

As discussed in the previous sections, dynamic SPRM of pancreatic beta-cells indicates an electrical origin for the synchronized oscillations observed among cells. Furthermore, the synchronization of these oscillations was quantitatively assessed using Pearson's correlation coefficient. This observation is supported by the well-established knowledge of coordinated electrical signaling in pancreatic cell networks[49,53]. This section presents a further investigation of connectivity between cells employing concepts from graph theory.

Functional connectivity was assessed using phase locking factor which was calculated for all combinations of the cell regions in the brightfield and the SPRM images in Fig. 8. Further details are provided in the Methods section. The results for the three experimental conditions are presented using the connectivity matrices, depicted in Fig. 8c and respective directed network graphs in Fig. 8d. These adjacency matrices and the directed graphs are examples extracted from the first 100 s of each treatment. A feedforward connectivity is observed extending spatially from cell 1 towards cell 6, as indicated by the upper triangle in the adjacency matrices. Additionally, Fig. 8c shows that cell 5 is only weakly connected to the other network nodes across all three treatments. This is unsurprising, as the cell exhibits weaker oscillatory activity compared with the others, as confirmed by Fig. 5c. Furthermore, the connectivity dynamics were investigated for each treatment, as presented in Fig. 8e. Both phase locking factor (PLF) and amplitude correlation coefficient (ACC) were calculated over a sliding 10-s window, stepped by one second. PLF was calculated as described in the Methods section while ACC was computed by first applying the Hilbert transform to each time series followed by smoothing and then calculating undirected correlations between the resulting amplitudes. Examples of time series and their corresponding amplitude envelopes are presented in Fig. 8e(i) to e(iii).

Figure 8f displays boxplots of the observations of the mean PLF and the mean ACC reported in Fig. 8e. First, we observe, from Fig. 8f(i) and f(ii), a drop in both PLF and ACC upon exposure to nifedipine in comparison to baseline and glucose supplemented HBSS. Second, while ACC does not change before and after exposure to glucose, PLF drops significantly and upon exposure to glucose. This observation can be explained by inspecting Fig. 8e(ii). When cells are exposed to glucose, network dynamics show an anticorrelation between the ACC

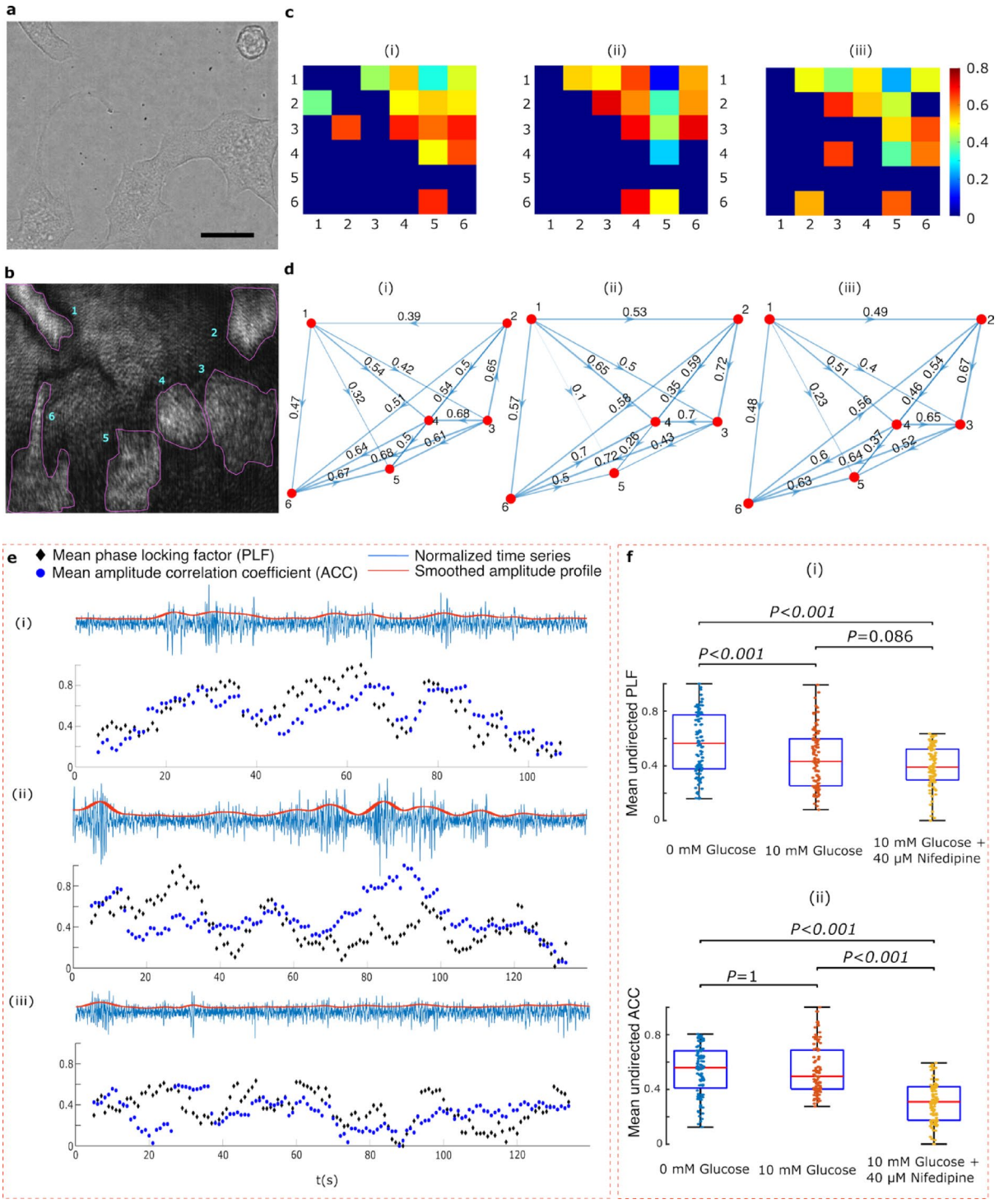

and PLF. While the amplitude envelopes are correlated during burst of activity, the cells undergo temporary, yet recoverable, phase decoherence (i.e. a drop in PLF), suggesting that connectivity drops temporarily during bursts. This observation indicates that cells burst in synchrony but, their individual spikes are incoherent[54]. These results demonstrate the capability of SPRM to reveal the connectivity and dynamics of living cell networks in a label-free manner. Quantifying synchronization through phase and amplitude measures offers a label-free method for assessing coordinated network behaviour, with potential applicability across cell types exhibiting varying degrees of connectivity and synchronization. The ability to observe and manipulate networks over extended periods, enabled by label-free approaches, is crucial for advancing research in several fields such as regenerative medicine, cancer, and neuroscience.

Discussion

The advancements in electronics, materials, nanotechnology and optics have led to bioelectric discoveries at multiple scales from single ion channels to macro brain circuits. However, method development research is still in

◀**Fig. 8**. Network analysis. (**a, b**) Brightfield and SPRM images of MIN6 cells, respectively. Scale bar 10 μm. (**c**) Connectivity matrices for the following conditions: baseline HBSS (**c.i**), HBSS supplemented with 10 mM glucose (**c.ii**) HBSS supplemented with 10 mM glucose and 40 μM nifedipine (**c.iii**). (**d**) Corresponding directed graphs represent cells ROIs as nodes, with edges (i.e. arrows) indicating patterns of directional connectivity and their associated weights. (**e**) Panels e(i) to e(iii) show examples of time series and their associated amplitude envelopes. Time-resolved connectivity, is presented for each of the above experimental conditions, measured via phase locking factor (PLF) and compared to amplitude correlation coefficient (ACC). PLF was calculated for a 10-s window with one second overlaps, for all cells and for each treatment. Similarly, ACC was computed by obtaining undirected correlation between the amplitude envelopes. (**f**) Boxplots depicting the mean undirected PLF (i) and the mean ACC (ii), calculated from their respective dynamic observations and averaged across six cells, are presented in panels e(i) and e(ii). In each boxplot, horizontal lines indicate the median values, while the boxes represent the IQR. Whiskers extend to 1.5 times the IQR. Paired t-tests were performed for multiple comparisons, with all P-values adjusted using the Bonferroni correction.

demand to overcome the current technological limitations enabling label-free tracking of cell electrical signaling with high resolution and high spatial sampling. This work introduces a novel surface plasmonic method to study living cell networks in a minimally invasive manner, for the first time. Surface plasmonic imaging can reveal subtle changes in optical properties at the cell sensor interface, under the perturbation of ionic flow. Therefore, plasmonic imaging has created avenues for monitoring electrical properties of cells and biomolecules as well as electrical signaling in neurons[16] and cardiac myocytes[17]. The results reported here demonstrate the ability to track electrical signaling from the subcellular level with a resolution of 1μm (Fig. 4) to a network level (Figs. 5 and 8), allowing a thorough investigation of information propagation within the network (Fig. 8). A small network of pancreatic beta-cells has been investigated to demonstrate the concept. The technique reveals highly correlated bioelectric signaling among cells, which is suppressed upon exposure to calcium channel blocker nifedipine (Fig. 5). When combined with graph theory, network structure and associated dynamics are uncovered. SPRM offers an ultra-high density recording capability (Fig. 4b(i)) and fine-grained imaging with a high spatial resolution down to 1 μm^2 (Fig. 4d) that is not currently possible with the widely used microelectrode arrays. The optical readout offered by SPRM further eliminates the need for complex electrical wiring of recording channels. Furthermore, SPRM creates the opportunity to integrate complementary microscopy techniques to maximize the retrieval of bioelectric information and its morphological and biochemical correlates. Additionally, SPRM offers a high temporal resolution of several kHz, that is limited only by the speed of the 2D detectors and therefore can track fast voltage membrane dynamics. Several research directions are focussed at enhancing SPRM sensitivity and information retrieval through active plasmonics[55,56], merging AI and plasmonics[57], and metamaterials[58], promising further advancement in SPRM imaging of electrical signaling. Furthermore, future studies may consider performing simultaneous imaging of electrical activity and calcium dynamics by integrating MEAs, patch-clamp techniques, $Ca2^{+}$ imaging, and SPRM. This approach, combined with bespoke computational models, would enable direct comparisons, potentially revealing both the limitations and the complementary strengths of each technique.

Bioelectric signaling plays a key role in regulating living processes with cells forming complex bioelectric networks. For instance, functional neuronal networks are linked to behaviour, memory, cognition and bidirectional communications with internal and external environments. Decades of electrophysiological discoveries present several examples of bioelectric control of living processes such as homeostasis of blood glucose concentration. Corradiated electrical signaling in pancreatic beta-cells, within the islet of Langerhans, underlies the secretion of insulin sufficient to restore equilibrium. Pancreatic islets function as intelligent organoids, with integrated glucose sensing and insulin secretion (i.e., actuation) mechanisms to main homeostatic balance where organoid-level computations are orchestrated by electric signaling. This work leverages the SPRM recordings to investigate pancreatic beta-cell networks (Fig. 8). Phase locking factor, when applied to the obtained signals, shows a strong functional connectivity which is altered under exposure to the calcium channel blocker nifedipine. The technique can also resolve dynamics of networks connectivity and its relations to the amplitude (i.e. envelope) of oscillations.

Label-free monitoring of bioelectric networks promises long-term tracking of connectivity promising to expose the regeneration[59] and cognitive[60] correlates. Discoveries of leading research groups have shown the important role of bioelectricity in cancer metastasis[8,61], with cancer cells exhibiting fluctuation in membrane potential, similar to excitable cells, demonstrated with electrochromic voltage-sensitive dye[7]. This study by Quicke et al., reported an intercellular correlation of V_m hyperpolarisation among cells, which hints to the importance of coordinated electrical communication. Furthermore, intercellular communication via depolarising potassium ion flow is linked to metabolic activity in bacterial biofilms[9]. The ability to monitor living cell networks under different chemical, optical and bioelectronic stimuli creates a myriad of opportunities for engineering living networks with applications in drug discovery, bioelectronics[62,63], regenerative medicine[59] and computing[64,65].

SPRM can track signal propagation beyond cells, as presented in Figs. 2, 4 and S3. In this study, highly correlated oscillations beyond cells were observed that are likely produced due to constructive interference of cell-generated signals. This capability is important when studying long-range and extracellular communication between cells[66] and elucidating the effects of electric field on cell excitability[67], migration[68] and regeneration[69]. The ability to image bioelectrical fields could enable a thorough investigation of different electrical pathways such as gap junction and extracellular routes in intercellular communications.

Methods

Simulations of SPR of cell-sensor interface

Transfer matrix method, a widely used method for studying light propagation in layered structures, was used to simulate the excitation of SPs given the variations in refractive index of the adhered sample. The cell sensor interface was studied using 1D model where light propagates through the following layers in the following order: glass (semi-infinite medium, n = 1.5133), thin film of gold (50nm, n = 0.13322 + i3.9722)[70], a cell medium gap between the cell membrane and the gold (thickness = 50 nm, n = 1.3350)[71], the cell membrane (thickness of 7.5 nm[72], n = 1.4985[73]) and cytosol being a semi-infinite (n = 1.36)[74]. The extracellular background with no cells present was modelled as glass, gold and semi-infinite cell medium having the same parameters mentioned above. SPR curve for both cells and their background were then calculated, at a wavelength of 690nm, by varying the angle of incidence in the range of (65° to 80° in steps of 0.01°) and calculating the resulting reflection coefficients.

Cell culture

The mouse pancreatic cell line, MIN6 (Beta-TC-6, ATCC; CRL-11506), was maintained in high Glucose DMEM (Merck, D5671) supplemented with 10% FBS (Merck, F9665), 10 mM HEPES (Merck, R0887), 50 mg/ml penicillin and streptomycin (Merck, P0781) and 50 mM b-mercaptoethanol (Merck, M3148). Cells of passage numbers 35–42 were incubated in a humidified atmosphere containing 5% CO2 at 37^0 C. 24h prior to electrical measurement, MIN6 cells were transferred to RPMI 1640 media (Merck, R0883) supplemented with 11 mM glucose (Merck, G8644), 10% FBS, 10 mM HEPES, 50 mg/ml penicillin and streptomycin. Gold-coated or glass coverslips (diameter 22mm) were coated with 0.01% PLL (Merck, P04707) as described by the manufacturer to aid cell adhesion. Cells we seeded at a density of 10^5 cells per coverslip in RPMI medium.

SPR microscopy of pancreatic beta-cells

The label-free imaging of pancreatic beta-cell networks in this study was conducted using a Kretchmann-Raether configuration that is detailed in our previous study[41]. Briefly, this setup is built around a high numerical aperture oil immersion objective lens (Nikon 60 × NA 1.49). This objective lens is configured to illuminate the sample at a fixed angle of incidence using a collimated linearly polarized coherent light source (690nm, fiber-coupled, 5 mW at the fibre output). The fixed angle illumination is achieved by focusing light onto the back focal plane (BFP) of the objective lens. A tube lens is positioned at distance equal to the sum of its focal length and that of the objective lens, transforming the intensity of the BFP into an image of the sample, which is captured by a 2D camera (SV643M, EPIX, Inc., IL, US). The angle of incidence can be scanned by laterally translating the focus on BFP. For this purpose, the BFP of the objective is imaged to confirm the excitation of the SPs and optimize the measurement conditions. The microscope and optical table were grounded to prevent electromagnetic interference.

The SPR sensor structure consisted of a 50 nm gold thin film deposited on a glass coverslip, with a 50 nm indium tin oxide (ITO) underlayer to enhance adhesion to the glass. All layers were deposited using magnetron sputtering. After 24h growth, MIN6 cells seeded on gold-coated glass coverslips were removed from RPMI growth medium and placed in a static bath to obtain baseline recordings containing HBSS with the following composition (in mM): 137 NaCl, 5.6 KCl, 1.2 $MgCl_2$, 2.6 $CaCl_2$, 1.2 NaH_2PO_4, 4.2 $NaHCO_3$ and 10 HEPES (pH 7.4 with NaOH). The bath was then replaced sequentially with HBSS supplemented with 10mM glucose prepared using a 1 M stock solution in water (10 µl/ml) followed by HBSS containing 40µM Nifedipine (Sigma), prepared from a 20 mM stock of Nifedipine in DiMethylSulfOxide. All experiments were conducted at 37°C.

Cells, under different treatments conditions, were monitored at frame rate of 100 Hz and exposure time of 0.5 ms and the acquired videos were post-processed using Matlab. Time series were obtained by integrating the intensity over a manually defined region of interest marking a cell, which were used to investigate connectivity. Time series were also extracted from ROIs as small as 1µm. The signals are filtered using a bandpass zero-phase Butterworth filter described below. Correlation between the time series was calculated using Pearson's correlation coefficient described in the next section.

Intracellular calcium imaging

MIN6 Cells were loaded with FLUO-4 and excited at 450–490 nm. The emitted light was band-pass filtered at 515–565 nm and captured at 12.5 Hz with a Coolsnap HQ2 camera (Photometrics, Tucson, AZ, USA) with Imaging Workbench (Ver. 6.2, INDEC Biosystems: RRID:SCR_016589). A circular region of interest with a diameter was drawn around each cell indicated and its average fluorescence calculated for that time point. Cells were continuously perfused at 32 °C in HBSS.

MEA recordings

50k MIN6 cells were seeded into each well of 24-well Axion Maestro MEA plates pre-coated with 0.01% PLL and 10 µg/ml fibronectin to enhance adhesion and SNR. To mimic fasting (no glucose), media was replaced with HBSS for 1 h, followed by HBSS + 10 mM glucose (30 min) and then HBSS + 10 mM glucose + 2 µM nifedipine (30 min). Signals were acquired on an Axion Maestro MEA system (16 electrodes/well) at 12.5 kHz per electrode. A lightweight preprocessing step suppressed baseline drift and high-frequency noise using a 4th-order zero-phase Butterworth bandpass filter (0.1–15 Hz) to capture slow oscillations and calcium-related field potentials. To examine spectral energy and visually separate activity components, additional sub-band filters (0.1–1 Hz, 1–10 Hz, 10–15 Hz) were applied with identical characteristics. Filtered signals were downsampled to 400 Hz for efficient plotting while preserving waveform fidelity.

Cell-attached patch-clamp recordings

MIN6 pancreatic beta cells were cultured in RPMI 1640 medium containing 11 mM glucose, 10% fetal bovine serum, 10 mM HEPES, and 50 µg/mL penicillin–streptomycin, and seeded onto glass coverslips 24 h before recording. Patch-clamp recordings were performed in the cell-attached configuration at 33 °C, with pipettes filled with 140 mM KCl-based solution and cells bathed in HBSS. Electrical activity was stimulated by 10 mM glucose, and nifedipine (10 µM) was applied following glucose stimulation. Currents were recorded via an Axoclamp 1B amplifier, filtered at 500 Hz, and digitised at 10 kHz. Spikes were detected in MATLAB using a dynamic, threshold-based method. Each segment (pre- and post-drug) was analysed separately. Baseline was the signal median, and noise was estimated via the median absolute deviation. Spikes were defined as downward deflections below baseline – 3 × noise, with a 50 ms refractory period to limit false positives.

Network analysis

Network analysis was performed in MATLAB 2023B (MathWorks). Code is available to download from the GitHub repository: github.com/dgalvis/sprm_bcell_networks. Time series data were collected as averages of the SPRM signal over 6 manually identified cellular ROIs. These time series were filtered between 1–15 Hz using a 4th order, zero-phase Butterworth filter. Unless otherwise noted, time series were then segmented into overlapping sliding windows of 10s – with a 1s increments (i.e., adjacent windows have a 9s overlap).

Phase locking factors (PLF) and amplitude-profile Pearson's correlation coefficients (ACC)[75,76] were calculated for each of the 10s segments to study changes in pairwise phase and amplitude correlation (respectively) over time and conditions (i.e., 0 mM glucose, 10 mM glucose and 10 mM glucose supplemented with 40 µM nifedipine). Calculation of PLF and ACC require application of the Hilbert transform to produce a complex-valued signal.

$$z\left(t\right) = R\left(t\right)e^{i\theta(t)}, \tag{1}$$

where $R(t)$ is the amplitude profile and $\theta(t)$ is the phase profile for the signal.

The pairwise PLF between signals i and j is given by.

$$c_{ij} = \left| \frac{1}{N} \sum_{n=1}^{N} e^{i\left(\theta_i(t_n) - \theta_j(t_n)\right)} \right|, \tag{2}$$

where t_n is the n th out of N sampling times. This method produces undirected networks, i.e., $c_{ij} = c_{ji}$, and we consider the undirected networks unless otherwise noted. However, this method can be made into directed network method by retaining the values of c_{ij}, if the angle of the complex number $\sum_{n=1}^{N} e^{i\left(\theta_i(t_n) - \theta_j(t_n)\right)}$ in Eq. 2 is positive, otherwise, $c_{ij} = 0$.

The pairwise ACC between signals i and j is given by.

$$c_{ij} = \frac{\sum_{n=1}^{N} \left(R_i\left(t_n\right) - \overline{R}_i\right)\left(R_j\left(t_n\right) - \overline{R}_j\right)}{N\sigma_{R_i}\sigma_{R_j}}, \tag{3}$$

where $\overline{R}_i, \overline{R}_j$ are the means and $\sigma_{R_i}, \sigma_{R_j}$ are the standard deviations of R_i and R_j, respectively. In both methods, self-connections are excluded, i.e., $c_{ii} = 0$.

To mitigate against spurious connections due to finite-length time series, 99 surrogate datasets for each time window were generated using the iterative amplitude-adjusted Fourier transform (IAAFT) method[77,78]. This method produces surrogate datasets that preserve autocorrelation whilst removing pairwise cross-correlations in the original signals. Using this method, a connection c_{ij} is rejected if it does not exceed the 95% level of significance (i.e., if $c_{ij} > s_{ij}$ in less than 95% of cases, where s_{ij} is the corresponding connection in a surrogate dataset). Where a connection is rejected, the connection is set to zero, i.e., $c_{ij} = 0$. Figure 8e shows the average connection strength over the network $\langle \mathrm{c\_ij} \rangle$ for each time window. Average ACC and PLF values were renormalized over all time windows and conditions such that the minimal and maximal values were 0 and 1, respectively.

Data availability

The datasets generated and analyzed during the current study are available as follows: Network analysis code is publicly available at [https://github.com/dgalvis/sprm/_bcell/_networks] (https:/github.com/dgalvis/sprm_bcell_networks). Network analysis was performed using MATLAB 2023B (MathWorks). Additional data (e.g., SPRM movies) generated during this study are available from the corresponding author upon reasonable request.

Received: 1 September 2025; Accepted: 24 December 2025
Published online: 03 January 2026

References

1. Ko, H. et al. The emergence of functional microcircuits in visual cortex. *Nature* **496**, 96–100 (2013).
2. Schneeberger, M., Gomis, R. & Claret, M. Hypothalamic and brainstem neuronal circuits controlling homeostatic energy balance. *J. Endocrinol.* **220**, T25–T46 (2014).
3. Xu, S. et al. Neural circuits for social interactions: from microcircuits to input-output circuits. *Frontiers in neural circuits* **15**, 768294 (2021).

4. Haraguchi, Y., Shimizu, T., Yamato, M., Kikuchi, A. & Okano, T. Electrical coupling of cardiomyocyte sheets occurs rapidly via functional gap junction formation. *Biomaterials* **27**, 4765–4774 (2006).
5. Stožer, A. et al. Functional connectivity in islets of Langerhans from mouse pancreas tissue slices. *PLoS Comput. Biol.* **9**, e1002923 (2013).
6. Watkins, S. C. & Salter, R. D. Functional connectivity between immune cells mediated by tunneling nanotubules. *Immunity* **23**, 309–318 (2005).
7. Quicke, P. et al. Voltage imaging reveals the dynamic electrical signatures of human breast cancer cells. *Communications Biology* **5**, 1178 (2022).
8. Peinado, P. *et al.* Intrinsic electrical activity drives small-cell lung cancer progression. *Nature* 1–11 (2025).
9. Prindle, A. et al. Ion channels enable electrical communication in bacterial communities. *Nature* **527**, 59–63 (2015).
10. Quintanilla, C. A. et al. High-density multielectrode arrays bring cellular resolution to neuronal activity and network analyses of corticospinal motor neurons. *Sci Rep* **15**, 732 (2025).
11. Obien, M. E. J., Deligkaris, K., Bullmann, T., Bakkum, D. J. & Frey, U. Revealing neuronal function through microelectrode array recordings. *Front. Neurosci.* **8**, (2015).
12. Xie, Y. et al. Materials and devices for high-density, high-throughput micro-electrocorticography arrays. *Fundamental Research* **5**, 17–28 (2025).
13. Dolenšek, J., Pohorec, V., Skelin Klemen, M., Gosak, M. & Stožer, A. Ultrafast multicellular calcium imaging of calcium spikes in mouse beta cells in tissue slices. *Acta Physiol.* **241**, e14261 (2025).
14. Johnston, N. R. et al. Beta cell hubs dictate pancreatic islet responses to glucose. *Cell Metab.* **24**, 389–401 (2016).
15. Kim, S. A., Kim, S. J., Moon, H. & Jun, S. B. In vivo optical neural recording using fiber-based surface plasmon resonance. *Optics Lett.* **37**, 614–616 (2012).
16. Liu, X. et al. Plasmonic-based electrochemical impedance imaging of electrical activities in single cells. *Angew Chem Int Ed* **56**, 8855–8859 (2017).
17. Habib, A. et al. Electro-plasmonic nanoantenna: A nonfluorescent optical probe for ultrasensitive label-free detection of electrophysiological signals. *Sci. Adv.* **5**, 9786 (2019).
18. Barry, J. F. et al. Optical magnetic detection of single-neuron action potentials using quantum defects in diamond. *Proc. Natl. Acad. Sci. U.S.A.* **113**, 14133–14138 (2016).
19. Hall, L. T. et al. High spatial and temporal resolution wide-field imaging of neuron activity using quantum NV-diamond. *Sci. Rep.* **2**, 401 (2012).
20. Balch, H. B. et al. Graphene electric field sensor enables single shot label-free imaging of bioelectric potentials. *Nano Lett.* **21**, 4944–4949 (2021).
21. Rothenhäusler, B. & Knoll, W. Surface–plasmon microscopy. *Nature* **332**, 615–617 (1988).
22. Yeatman, E. & Ash, E. A. Surface plasmon microscopy. *Electron. Lett. (UK)* **23**, 1091–1092 (1987).
23. Peterson, A. W., Halter, M., Tona, A. & Plant, A. L. High resolution surface plasmon resonance imaging for single cells. *BMC Cell Biol* **15**, 35 (2014).
24. Robelek, R. & Wegener, J. Label-free and time-resolved measurements of cell volume changes by surface plasmon resonance (SPR) spectroscopy. *Biosens. Bioelectron.* **25**, 1221–1224 (2010).
25. Campbell, C. T. & Kim, G. SPR microscopy and its applications to high-throughput analyses of biomolecular binding events and their kinetics. *Biomaterials* **28**, 2380–2392 (2007).
26. Wang, W. et al. Label-free measuring and mapping of binding kinetics of membrane proteins in single living cells. *Nat. Chem.* **4**, 846–853 (2012).
27. Moreira, B., Tuoriniemi, J., Kouchak Pour, N., Mihalcikova, L. & Safina, G. Surface plasmon resonance for measuring exocytosis from populations of PC12 cells: mechanisms of signal formation and assessment of analytical capabilities. *Analytical Chemistry* **89**, 3069–3077 (2017).
28. Ahn, H. et al. Plasmonic sensing, imaging, and stimulation techniques for neuron studies. *Biosens. Bioelectron.* **182**, 113150 (2021).
29. Abadian, P. N., Tandogan, N., Jamieson, J. J. & Goluch, E. D. Using surface plasmon resonance imaging to study bacterial biofilms. *Biomicrofluidics* **8**, (2014).
30. Boulade, M. et al. Early detection of bacteria using SPR imaging and event counting: experiments with Listeria monocytogenes and Listeria innocua. *RSC Adv.* **9**, 15554–15560 (2019).
31. Hemmerová, E. & Homola, J. Combining plasmonic and electrochemical biosensing methods. *Biosens. Bioelectron.* **251**, 116098 (2024).
32. Zhou, X.-L., Yang, Y., Wang, S. & Liu, X.-W. Surface Plasmon Resonance Microscopy: From Single-Molecule Sensing to Single-Cell Imaging. *Angew. Chem. Int. Ed.* **59**, 1776–1785 (2020).
33. Thadson, K., Visitsattapongse, S. & Pechprasarn, S. Deep learning-based single-shot phase retrieval algorithm for surface plasmon resonance microscope based refractive index sensing application. *Sci Rep* **11**, 16289 (2021).
34. Nizamov, S., Sazdovska, S. D. & Mirsky, V. M. A review of optical methods for ultrasensitive detection and characterization of nanoparticles in liquid media with a focus on the wide field surface plasmon microscopy. *Anal. Chim. Acta* **1204**, 339633 (2022).
35. Somekh, M. G., Liu, S., Velinov, T. S. & See, C. W. High-resolution scanning surface-plasmon microscopy. *Appl. Opt.* **39**, 6279–6287 (2000).
36. Tan, H.-M., Pechprasarn, S., Zhang, J., Pitter, M. C. & Somekh, M. G. High resolution quantitative angle-scanning widefield surface plasmon microscopy. *Sci. Rep.* **6**, 20195 (2016).
37. Huang, B., Yu, F. & Zare, R. N. Surface plasmon resonance imaging using a high numerical aperture microscope objective. *Anal. Chem.* **79**, 2979–2983 (2007).
38. Son, T. et al. Enhanced surface plasmon microscopy based on multi-channel spatial light switching for label-free neuronal imaging. *Biosens. Bioelectron.* **146**, 111738 (2019).
39. Toma, K., Kano, H. & Offenhäusser, A. Label-free measurement of cell–electrode cleft gap distance with high spatial resolution surface plasmon microscopy. *ACS Nano* **8**, 12612–12619 (2014).
40. Wang, W. et al. Single cells and intracellular processes studied by a plasmonic-based electrochemical impedance microscopy. *Nat. Chem.* **3**, 249–255 (2011).
41. Abayzeed, S. A. Plasmonic-based impedance microspectroscopy of optically heterogeneous samples. *Biomed. Opt. Express* **11**, 6168–6180 (2020).
42. Abayzeed, S. A., Smith, R. J., Webb, K. F., Somekh, M. G. & See, C. W. Sensitive detection of voltage transients using differential intensity surface plasmon resonance system. *Opt. Express* **25**, 31552–31567 (2017).
43. Potdar, P., Kharat, A., Sanap, A., Kheur, S. & Bhonde, R. Pancreatic β cell models for screening insulin secretagogues and cytotoxicity. *J. Appl. Toxicology* **45**, 89–106 (2025).
44. Dalle, S. et al. Miniglucagon (glucagon 19–29), a potent and efficient inhibitor of secretagogue-induced insulin release through a Ca2+ pathway. *J. Biol. Chem.* **274**, 10869–10876 (1999).
45. Ashcroft, F. M. et al. Stimulus-secretion coupling in pancreatic β cells. *J. Cell. Biochem.* **55**, 54–65 (1994).
46. Dean, P. M. & Matthews, E. K. Glucose-induced electrical activity in pancreatic islet cells. *J. Physiol.* **210**, 255–264 (1970).
47. Yang, S.-N. et al. Ionic mechanisms in pancreatic β cell signaling. *Cell. Mol. Life Sci.* **71**, 4149–4177 (2014).
48. Somekh, M. G., Regules-Medel, K. & Abayzeed, S. A. Common framework for surface plasmon binding and voltage sensing and microscopy with transmission line representation. *J. Opt. Soc. Am. A* **41**, C90–C98 (2024).

49. Quesada, I. et al. Glucose induces opposite intracellular Ca2+ concentration oscillatory patterns in identified α-and β-cells within intact human islets of Langerhans. *Diabetes* **55**, 2463–2469 (2006).
50. Pechprasarn, S. & Somekh, M. G. Surface plasmon microscopy: resolution, sensitivity and crosstalk. *J. Microsc.* **246**, 287–297 (2012).
51. Vasseur, M., Debuyser, A. & Joffre, M. Sensitivity of pancreatic beta cell to calcium channel blockers: an electrophysiologic study of verapamil and nifedipine. *Fundamemntal Clinical Pharma* **1**, 95–113 (1987).
52. Abayzeed, S. A., Smith, R. J., See, C. W. & Somekh, M. G. Analysis of noise in differential and ratiometric biosensing systems. *Sens. Actuators, B Chem.* **260**, 1059–1067 (2018).
53. Gresch, A. et al. Resolving spatiotemporal electrical signaling within the islet via CMOS microelectrode arrays. *Diabetes* **74**, 343–354 (2025).
54. Belykh, I. & Hasler, M. Mesoscale and clusters of synchrony in networks of bursting neurons. *Chaos: An Interdisciplinary Journal of Nonlinear Science* **21**, (2011).
55. Jiang, N., Zhuo, X. & Wang, J. Active Plasmonics: Principles, Structures, and Applications. *Chem. Rev.* **118**, 3054–3099 (2018).
56. Habib, A., Zhu, X., Fong, S. & Yanik, A. A. Active plasmonic nanoantenna: an emerging toolbox from photonics to neuroscience. *Nanophotonics* **9**, 3805–3829 (2020).
57. Malkiel, I. et al. Plasmonic nanostructure design and characterization via deep learning. *Light: Sci. Appl.* **7**, 60 (2018).
58. Moon, G. et al. Machine learning-based design of meta-plasmonic biosensors with negative index metamaterials. *Biosens. Bioelectron.* **164**, 112335 (2020).
59. Levin, M., Pezzulo, G. & Finkelstein, J. M. Endogenous bioelectric signaling networks: exploiting voltage gradients for control of growth and form. *Annu. Rev. Biomed. Eng.* **19**, 353–387 (2017).
60. Manicka, S. & Levin, M. Modeling somatic computation with non-neural bioelectric networks. *Sci. Rep.* **9**, 18612 (2019).
61. Fraser, S. P. et al. Voltage-gated sodium channel expression and potentiation of human breast cancer metastasis. *Clin. Cancer Res.* **11**, 5381–5389 (2005).
62. Tian, B. & Lieber, C. M. Nanowired Bioelectric Interfaces: Focus Review. *Chem. Rev.* **119**, 9136–9152 (2019).
63. Rivnay, J. *et al.* Integrating bioelectronics with cell-based synthetic biology. *Nature Reviews Bioengineering* 1–16 (2025).
64. Wang, Y. et al. An optoelectrochemical synapse based on a single-component n-type mixed conductor. *Nat. Commun.* **16**, 1–14 (2025).
65. Smirnova, L. et al. Organoid intelligence (OI): the new frontier in biocomputing and intelligence-in-a-dish. *Frontiers in Science* **1**, 1017235 (2023).
66. Scholkmann, F. Two emerging topics regarding long-range physical signaling in neurosystems: Membrane nanotubes and electromagnetic fields. *J. Integr. Neurosci.* **14**, 135–153 (2015).
67. Bikson, M. et al. Effects of uniform extracellular DC electric fields on excitability in rat hippocampal slices *in vitro*. *J. Physiol.* **557**, 175–190 (2004).
68. Funk, R. H. Endogenous electric fields as guiding cue for cell migration. *Front. Physiol.* **6**, 143 (2015).
69. Messerli, M. A. & Graham, D. M. Extracellular electrical fields direct wound healing and regeneration. *Biol. Bull.* **221**, 79–92 (2011).
70. Johnson, P. B. & Christy, R. W. Optical constants of the noble metals. *Phys. Rev. B* **6**, 4370–4379 (1972).
71. Kreysing, E., Hassani, H., Hampe, N. & Offenhäusser, A. Nanometer-resolved mapping of cell–substrate distances of contracting cardiomyocytes using surface plasmon resonance microscopy. *ACS Nano* **12**, 8934–8942 (2018).
72. Meyer, R. A. Light scattering from biological cells: dependence of backscatter radiation on membrane thickness and refractive index. *Appl. Opt., AO* **18**, 585–588 (1979).
73. Barer, R. & Joseph, S. Refractometry of living cells part I. basic principles. *Journal of Cell Science* **s3–95**, 399–423 (1954).
74. Schürmann, M., Scholze, J., Müller, P., Guck, J. & Chan, C. J. Cell nuclei have lower refractive index and mass density than cytoplasm. *J. Biophotonics* **9**, 1068–1076 (2016).
75. Lachaux, J.-P., Rodriguez, E., Martinerie, J. & Varela, F. J. Measuring phase synchrony in brain signals. *Hum. Brain Mapp.* **8**, 194–208 (1999).
76. Palva, J. M. et al. Ghost interactions in MEG/EEG source space: A note of caution on inter-areal coupling measures. *Neuroimage* **173**, 632–643 (2018).
77. Schmidt, H., Petkov, G., Richardson, M. P. & Terry, J. R. Dynamics on networks: the role of local dynamics and global networks on the emergence of hypersynchronous neural activity. *PLoS Comput. Biol.* **10**, e1003947 (2014).
78. Schreiber, T. & Schmitz, A. Improved surrogate data for nonlinearity tests. *Phys. Rev. Lett.* **77**, 635–638 (1996).

Acknowledgements

The authors acknowledge the financial support of the Engineering and Physical Sciences Research Council [EP/M50810X/1, EP/X018024/1], UKRI [MR/X034240/1], and the University of Nottingham. SA acknowledges the financial support of Nottingham Research Fellowship. DG acknowledges financial support from the University of Birmingham Dynamic Investment Fund.

Author contributions

SA (conception, SPRM experiments, data analysis, writing, editing, supervision), DG (network analysis, writing, editing), KRM (SPRM simulations, patch clamp experiments, writing), CFJ (MEA recordings, writing), OBG (sensor fabrication and characterisation), KS (cell culture optimization and viability, writing, editing), RM (MEA recording concept, supervision), MGS (SPRM concept, editing, supervision), KCAW (network analysis concept, writing, editing, supervision), PS (conception, writing, editing, supervision).

Funding

This work was supported by the Engineering and Physical Sciences Research Council [EP/M50810X/1, EP/X018024/1], UKRI [MR/X034240/1], the University of Nottingham and the University of Birmingham.

Declarations

Competing interests

The authors declare no competing interests.

Additional information

Supplementary Information The online version contains supplementary material available at https://doi.org/1

0.1038/s41598-025-34094-0.

Correspondence and requests for materials should be addressed to S.A.